Title

Seabed Wide-Angle Reflection Coefficient and Source Radiation Pattern Measurements From a Low-Frequency Multibeam Sonar

Journal

IEEE Journal of Oceanic Engineering, 51(3)

ISSN

0364-9059

Authors

Holland, Charles W
Henderson, Cody R
Sonnemann, Tim
et al.

Publication Date

2026-07-01

DOI

10.1109/joe.2026.3691004

Peer reviewed

This article has been accepted for inclusion in a future issue of this journal. Content is final as presented, with the exception of pagination.

Seabed Wide-Angle Reflection Coefficient and Source Radiation Pattern Measurements From a Low-Frequency Multibeam Sonar

Charles W. Holland, Cody R. Henderson, Tim Sonnemann, Bjørnar Langli, and Daniel L. Orange

***Abstract*—In acoustic remote sensing, the seabed frequency-domain reflection coefficient contains significant geoacoustic information, namely the depth and frequency dependence of sediment sound speed, density, and attenuation. Typical reflection measurements are performed with a towed source and/or receivers to obtain a range of seabed reflected angles. It is shown here that the measurements can be performed using a hull-mounted low-frequency multibeam sonar with an offboard fixed or drifting hydrophone. To obtain the reflection coefficient (as well as scattering strength and other quantities of potential interest), the multibeam sonar radiation pattern must be known. Radiation patterns and absolute levels of the Kongsberg SBP29 multibeam sonar are measured and reflection coefficient measurements are presented in two geologically dissimilar environments, the Eel River shelf, CA and the Santa Barbara Basin, CA. The reflection coefficient frequency and angle dependences are explored via forward modeling to determine regions of the data space that contain information about the geoacoustic properties.**

***Index Terms*—Geophysical measurement techniques, sediments, sonar applications.**

I. Introduction

KNOWLEDGE of seabed and subseabed properties is important for a wide range of scientific and commercial enterprises. For example, the seabed holds a record of Earth's history and the geological processes that have shaped it. As another example, the undersea soundscape, important for marine life, is often controlled by the properties of the seabed. Design and placement of offshore structures, as well as submarine cable laying, also depend upon knowledge of seabed properties.

While there are many ways to measure seabed properties, all have limitations of one kind or another. In the world of remote acoustic sensing, one way is to infer them from a measurement of the wide-angle frequency-domain seabed reflection coefficient. This quantity has been shown to have high geoacoustic information content, e.g., as presented in [1]. Geoacoustic properties in this article mean sediment sound speed, density, and compressional wave attenuation as a function of depth and frequency.

The objective of this work is to determine the feasibility of measuring the reflection coefficient using a hull-mounted commercial multibeam sonar and a single offboard receiver. Why is making such measurements with a multibeam sonar important, as opposed to other sources used in the past? First, because of the simplicity of a hull-mounted source—no towed sources or receivers are required. Second, the multibeam used here, the Kongsberg SBP29, has a broad bandwidth, 2–9 kHz. This is significant because geoacoustic information content generally increases with increasing bandwidth. Third, this multibeam is rapidly becoming more widely available to the scientific community.

To measure the wide-angle frequency-domain seabed reflection coefficient, hereafter termed simply reflection coefficient, or R, the source radiation pattern as a function of frequency must be accurately known. Thus, as a foundation of this work, the absolute source levels of the SBP29 sonar are measured for various transmit (TX) modes. The article is broadly organized by first presenting the SBP29 radiation pattern and then the reflection coefficient.

In Section II, the SBP29 transmitter is described along with the approach for the radiation pattern measurements and modeling. The radiation pattern measurement results are then presented for two TX modes. In Section III, the reflection coefficient measurement and modeling approaches are described. Reflection coefficient measurement results are then presented and modeling is employed to interpret the measurements and their sensitivity to the geoacoustic properties at two geologically distinct sites. It also provides a discussion on other measurement quantities that can exploit the radiation pattern results. Finally, Section IV concludes this article. The Appendix provides along-track and cross-track radiation patterns for additional SBP29 TX modes, potentially useful for other geoacoustic inversion approaches.

II. SBP29 Transmit Measurements and Modeling

This section presents the SBP29 transmitter design and characteristics, followed by measurement and modeling approaches. Finally, measured and modeled radiation patterns are presented.

Received 3 July 2025; revised 3 March 2026; accepted 13 April 2026. *(Corresponding author: Charles W. Holland.)*

Associate Editor: Z.-H. Michalopoulou.

Charles W. Holland and Tim Sonnemann are with the Department of Electrical and Computer Engineering, Portland State University, Portland, OR 97201 USA (e-mail: charles.holland@pdx.edu).

Cody R. Henderson is with Norbit, Portland, OR 97232 USA.

Bjørnar Langli is with Kongsberg Discovery, 3183 Horten, Norway.

Daniel L. Orange is with the Department of Earth and Planetary Sciences, University of California, Santa Cruz, CA 95064 USA.

Digital Object Identifier 10.1109/JOE.2026.3691004

This article has been accepted for inclusion in a future issue of this journal. Content is final as presented, with the exception of pagination.

Fig. 1. SBP29 transmit modes as they became available by year. Each square represents a single transmit element. The manufacturer's original options are shown in the left panel (2001). The additional transmit modes requested for scientific purposes are shown in panels to the right.

A. SBP29 Transmitter

The SBP29 is a low-frequency, 2–9 kHz, multibeam subbottom profiler. The source consists of 96 elements arranged in three 32-element columns mounted on the hull of the ship in the along-track direction. The transmit (TX) elements are MASSA TR-1447, which have identical dimensions but different tuning than the more widely available TR-1075 [2] used in the Knudsen subbottom profiler.

The TX element spacing along-track and cross-track is 0.226 m and 0.1872 m, respectively. Thus, the length is 7 m and the width is 0.56 m. For along-track elements, the manufacturer uses Chebyshev spatial weighting [3] with sidelobes selected at −30 dB. For cross-track elements, the outer two columns are driven at half-power relative to the central column. The along-track full aperture (32 elements) gives a nominal along-track 3-dB beamwidth of 3° at 4 kHz and at half-aperture (16 elements) 6°. Henceforth, the term "aperture" refers to the along-track dimension.

The original TX modes are shown in the left three diagrams of Fig. 1 labeled 2001. To increase the cross-track beamwidth for interval velocity estimation [4] and cross-track mapping [5], we requested a single (central) column TX mode for all three apertures (labeled 2021) with the outer columns clamped. We subsequently requested a new shorter aperture, three elements (2022), and most recently a single-element TX capability (2024).

B. Radiation Pattern Measurement Approach

1) Experiment Design: The main calibration experiment took place in the San Diego Trough from July 3–5, 2021. A mooring was deployed at 33° 2.391′ N, 117° 58.391′ W in 970-m water depth with a calibrated hydrophone (Ocean Sonics ICListen SC35-ETH) at 898-m depth. This large receiver depth reduces amplitude and angular errors due to small positional uncertainties and is well beyond the far field of full-aperture transmissions, i.e., ∼300 m.

The survey pattern was designed to yield an equiangle spacing in the cross-track direction, with an angular resolution of 5° (see Appendix). The 6-km line length, with the receiver placed at ∼4 km yields along-track source angles from −87° to 55°. The along-track angular resolution is dictated by the pulse rate and ship speed. For a constant pulse rate and ship speed, the angular resolution varies monotonically in the along-track direction from ∼1° at nadir to ∼0.1° at 80°.

The radiation pattern was measured for four different TX modes, full and half-apertures for both three TX (3TX) columns and one TX (1TX) column. To measure the radiation pattern with sufficient angular resolution, only two modes could be performed at a time. This was accomplished by first conducting the survey for the 1TX case, interleaving the full and half-apertures with a down- and up-chirp signal, respectively, each at 1/6 Hz pulse repetition rate, separated by 3 s. This pulse repetition rate, 1/6 Hz, was necessary to minimize interference from multipaths. In particular, this prevented multipath arrivals from the full aperture biasing the (lower source level) half-aperture measurements, especially in the sidelobes. The 1TX survey took ∼20 h, following which the survey lines were repeated with the 3TX full- and half-apertures with the same pulse train. The broadcast signal was an 80 ms linear frequency modulated (LFM) chirp from 2–9 kHz.

Along-track radiation pattern measurements from single array elements were conducted in fall 2024. The minimum distance between source and receiver was 75 m; the far-field requirement is less than 1 m from the source. The transmitted pulse was a 100 ms LFM at a 1-Hz pulse repetition rate.

2) Data Processing: The data processing is first described for measurements at the closest point of approach (CPA) followed by that for the general radiation pattern. The motivation for the two processing methods was that at CPA, the direct path was fully separable from the bottom reflected path, such that simple processing could be performed, i.e., without using a matched filter. This provided a useful check for the general case where the matched filter was needed.

a) CPA processing: At least one line on each survey traversed directly or nearly directly over the mooring. For each TX mode, CPA was determined by the ping with the highest direct path amplitude. The source levels in units of dB re 1 μPa @ 1 m were obtained from

$$\mathrm{SL_{CPA}}\,(\mathrm{f}) = 20\log_{10}\left(V_{\mathrm{RX}}\,(f)\,/s\,(f)\right) + 20\log_{10}(\gamma) + L\,\alpha\,(f) \quad (1)$$

where V_{RX} is the rms voltage from the calibrated hydrophone, computed by taking the envelope of the bandpass filtered direct path arrival time series divided by $\sqrt{2}$. The function s is the sensitivity in V/μPa, which was interpolated linearly from 26 to 10 kHz (but varied only by 0.75 dB across that range). The term γ is the calculated pressure ratio of the source radiated pressure at 1 m and the received pressure. At CPA, $\gamma = L/1$ m, the length of the direct path connecting source and receiver in meters. α is the seawater attenuation [6] in decibels per meter. While seawater attenuation is a function of depth, the difference between integrating it over depth and simply multiplying L by the average attenuation between source and receiver was small, a fraction of a decibel.

The uncertainty of the first term from the manufacturer (Ocean Sonics), considering slight aging of the ceramic, is less than ± 1 dB. The uncertainty associated with the second term, depth L, is less than 0.1 dB, and the third term uncertainty is about 0.1 dB. Thus, the total measurement uncertainty is about ± 1 dB.

The processing operates on band-passed time series data. Determining the pulse start or end by inspection is error-prone since the temporal shading applied to the pulse transmission (in this case, very similar to a 10% Tukey window) leads to a low signal-to-noise ratio (SNR) at the start and end. Turn ON and turn OFF transients can compound the problem. Instead, the instantaneous frequencies (with MatLab function *instfreq* [7]) are found at times where the SNR is sufficiently high, the envelope is computed and convolved in time (smoothed) with a 0.86 ms boxcar function.

b) General: The approach described above is limited to cases where there is no multipath interference. This means that the seabed reflected path must arrive later than one pulse length (80 ms duration) after the direct path or a distance of $\sim$120 m. Since the hydrophone is 70 m above the seabed or a 2-way distance of 140 m, (1) suffices for angles near normal incidence. But at most horizontal offsets from the receiver, the time between multipath arrivals is less than the pulse length. In this case, matched filtering is employed to separate the direct and bottom reflected paths. The Bellhop ray model [8], [9] was employed to predict γ the path length L.

The on-axis source level, $\mathrm{SL_{axis}}$, is virtually identical to $\mathrm{SL_{CPA}}$ when the beamwidth is broad. However, this will not be true for a narrow beampattern. We can write their difference,

$$\begin{aligned}\mathrm{SL_{axis}} - \mathrm{SL_{CPA}} &= B(0,0,f) - B(\theta_{\mathrm{CPA}}, \phi_{\mathrm{CPA}}, f)\\ &= -\,B(\theta_{\mathrm{CPA}}, \phi_{\mathrm{CPA}}, f)\end{aligned}$$

where B is the normalized theoretical beampattern (0 dB at nadir) and θ and ϕ are the vertical and azimuthal angles, respectively, with $\theta = 0°$ at nadir $\phi = 0°$ in the along-track direction. Thus, the on-axis source level is given by

$$\mathrm{SL_{axis}}\,(f) = 20\log_{10}\left(V_{\mathrm{RX}}\,(f)\,/s\,(f)\right) + 20\log_{10}(\gamma) + L\,\alpha\,(f) - B\left(\theta_{\mathrm{CPA}}, \phi_{\mathrm{CPA}}, f\right). \quad (2)$$

As an example, at $\theta_{\mathrm{CPA}} = 1.5°$ and half-aperture at 2.5 kHz, $-B = 0.2$ dB and at 8.5 kHz, $-B = 2.8$ dB. In other words, it is expected that at the lower sonar frequencies, the SL difference between CPA and on-axis will be small, but not negligible at higher frequencies.

C. Radiation Pattern Modeling

Modeled source levels are indicated by $\widehat{\mathrm{SL}}$. For the on-axis response, it is

$$\widehat{\mathrm{SL}}_{\mathrm{axis}}\,(f) = \mathrm{TVR}^{m}\,(f) + 20\log_{10}\left(V_{\mathrm{TX}}\right) + 20\log_{10}\left(\sum_{m=1}^{M} w_m^{\perp} \sum_{n=1}^{N} w_n^{-}\right) \quad (3)$$

where V_{TX} is the rms voltage applied to the transmitter, $M = 1$ or 3 is the number of transmitters in the cross-track direction, and the cross-track weights are $w^{\perp} = \left[\sqrt{2}^{-1},\ 1,\ \sqrt{2}^{-1}\right]$, for 1TX, $M = 1$, $w^{\perp} = 1$;$N = 16$ or 32 is the number of transmitters in the along-track direction for half-aperture and full aperture, respectively, and along-track weights w^{-} are a Chebyshev shading with -30 dB sidelobes.

The TX voltage response measurements, TVR^{m}, were conducted by the manufacturer (MASSA), averaging over individual transmitters. The measurement and averaging uncertainty of TVR^{m} is unknown. The uncertainty associated with the second term of (3) is also unknown, but its uncertainty and that of the third term should be small relative to that of the first term. In other words, the total uncertainty of $\widehat{\mathrm{SL}}_{\mathrm{axis}}$ is likely dominated by measurement uncertainty in the first term and in particular, the variability of individual elements (see Section II-D1).

The modeled source level for the general case, including off-axis, is essentially the same, but exploits the measured on-axis spectral characteristics $\mathrm{SL_{axis}}$ and includes the frequency and vertical angular dependence of an individual TX element, *p(f,θ),* where $\dot{p}$ is normalized to unity at nadir,

$$\widehat{\mathrm{SL}}\,(f,\theta,\phi) = \mathrm{SL_{axis}}\,(f) + 20\log_{10}\left(\dot{p}\,(f,\theta)\right) + B\,(f,\theta,\phi) \quad (4)$$

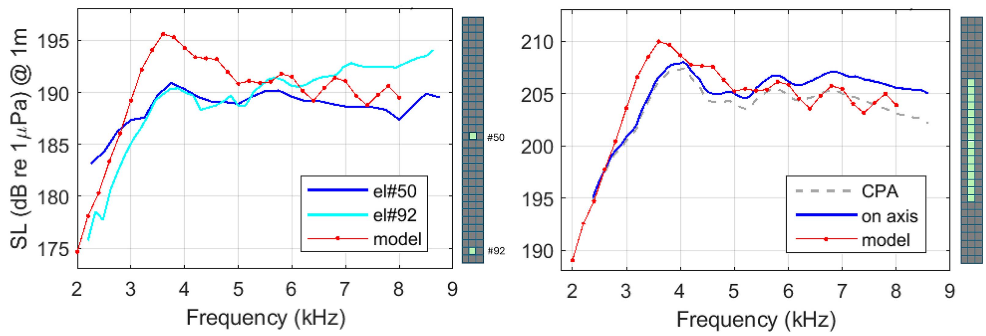

(a) (b)

Fig. 2. On-axis source level measurements and model. (a) Single elements at 110 $\mathrm{V_{rms}}$. (b) 1TX column half-aperture at 55 $\mathrm{V_{rms}}$. The panel to the right of each plot shows the active transmit elements of the SBP29 sonar.

where B is the theoretical far-field array beampattern with a 200 Hz band frequency average in intensity, commensurate with the 200 Hz bandwidth of measurements $\mathrm{SL_{CPA}}$ and $\dot{p}$.

D. Measured and Modeled Radiation Patterns

In this section, measured on-axis and off-axis radiation pattern measurements are presented and discussed along with model results.

1) On-Axis Source Level Frequency Dependence: Measurements of on-axis source level are shown first for a single TX element, which is the most relevant for the reflection coefficient measurements. The radiation pattern is sufficiently broad and the pulse repetition rate sufficiently high, that CPA is on the axis of the transmitter.

Single-element transmissions were measured in August and September 2024 for two different elements, TX #50 near the array center and #92 the penultimate element at the aft end. The measured on-axis source level for single-element transmissions are shown in Fig. 2(a). Both elements behave similarly at their resonance ∼3.8 kHz, though their spectral trends differ. The highest SL is at resonance for #50 as expected; however, #92 exhibits its peak SL at 8.6 kHz, not at resonance. The low-frequency SL also differs, at 2250 Hz #50 yields a 7 dB higher SL than #92. Several adjacent pings were processed, which gave similar results.

The main takeaway is that there is considerable SL variability from element-to-element, which indicates a nonnegligible TVR^m uncertainty, i.e., a nonnegligible model uncertainty. Model results in Fig. 2(a) predict a lower resonance frequency, 3.6 kHz, and a higher SL at resonance by ∼5 dB. The model frequency dependence above resonance generally decreases with frequency, whereas the two individual elements are either flat or increase with frequency.

The measured 1TX SL data are presented in Fig. 2(b) for the half array aperture. The measured resonant frequency occurs at a higher frequency, ∼4 kHz, than that of the TVR^m, but lower in amplitude. Also, the frequency dependence above resonance does not roll off like that of the TVR^m. These trends are all broadly similar to those of the single elements.

The half-aperture on-axis measurements have uncertainties from both the CPA (±1 dB) and an uncertainty associated with the CPA angle used to estimate the on-axis response. That angle uncertainty leads to a frequency-dependent uncertainty that is a fraction of a dB at 2.5 kHz and increases to an estimated ±1 dB at 8.5 kHz.

With on-axis measured SL, it is possible to measure the normal incidence reflection coefficient, as in [10] (using the SBP array, not a single element). However, to measure its reflection coefficient angular dependence, which contains substantially more geoacoustic information, the radiation pattern must be measured, as discussed in the following.

2) Along-Track Radiation Patterns

Along-track radiation pattern measurements from a single element, #50, are shown in Fig. 3. The data generally show SL decreasing monotonically with increasing angle. One notable exception to the monotonic behavior is the 8 kHz pronounced dip at ∼45°. By way of comparison, beamwidth measurements were reported [11] from a similar model, the TR-1075, with identical dimensions and different tuning. Their measurements showed beamwidths of about 80° and 180° at − 3 and −10 dB, respectively, at 4 kHz. The SBP29 TR-1447 at 4 kHz has beamwidths of about 110° and 140°, respectively.

The TX elements are indicated by the manufacturer (MASSA) to function as a "true piston radiating source". The dashed lines in Fig. 3 are predictions for a baffled rigid circular piston (e.g., as presented in [12]) with radius $a = 9.2$ cm, the actual dimension. The piston beampattern has been normalized here to the measured SL value at nadir to facilitate comparisons between model and data. From 3–7 kHz, the model reasonably captures the data from 0°–45°; but at larger angles, it substantially overpredicts the SL. It also poorly predicts the SL below 3 kHz and above 7 kHz.

It is clear that the piston model is not a good representation of the TX element. The data show much greater angle dependence than the model predicts, tens of dB at high angles. If a (unreasonably) larger piston radius is used, $a = 16$ cm, the predictions are still poor.

The measured along-track SL for 1TX at half-aperture is shown at various frequencies in Fig. 4 along with the model predictions (cyan). These provide an opportunity to examine peak levels on axis and at grating lobes, beamwidths, and sidelobe levels.

Note that the measured beamwidths of the main lobe accord well with those predicted using the known parameters of the

This article has been accepted for inclusion in a future issue of this journal. Content is final as presented, with the exception of pagination.

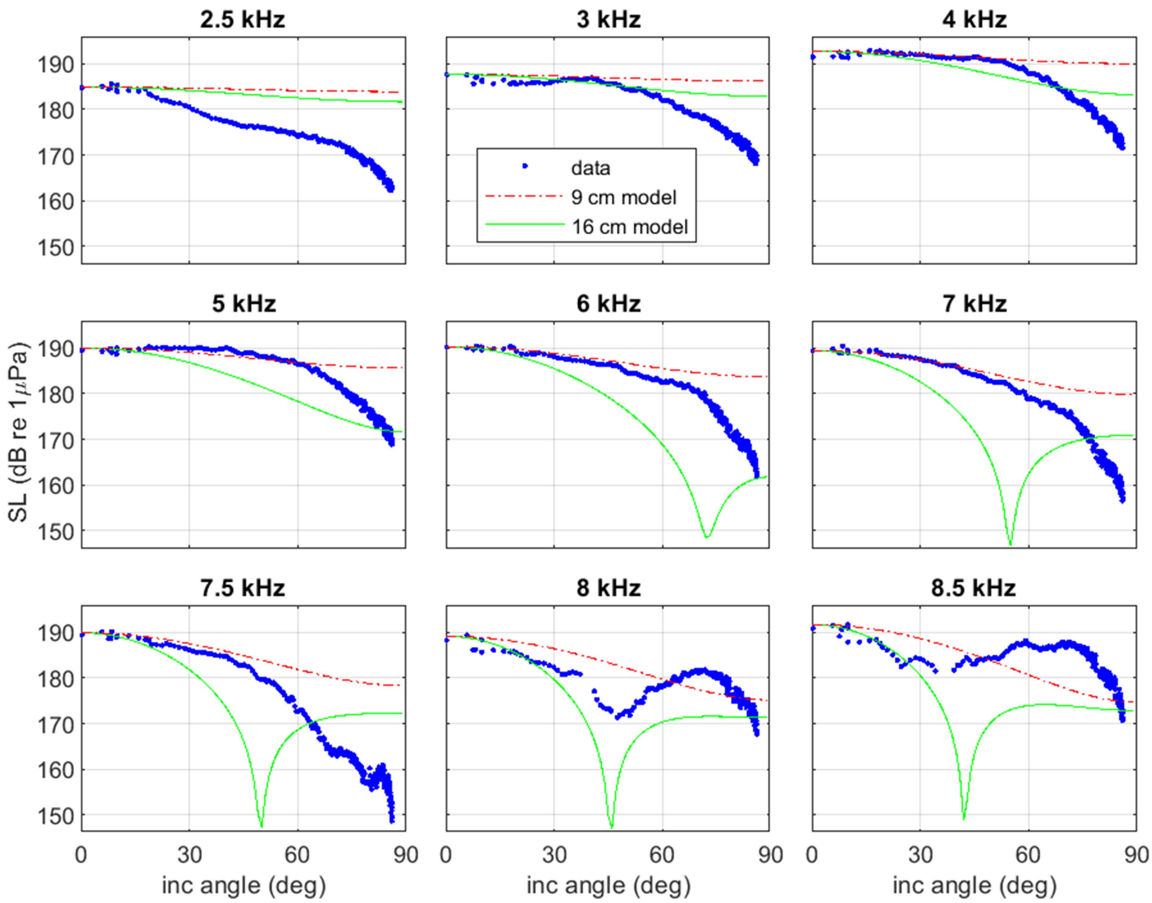

Fig. 3. Single-element (#50) source level measurements (•) at 110 V_{rms} and a model of the element as a baffled piston with the actual element radius 9 cm (— · —) and larger, 16 cm (—).

transmitter. Grating lobes are observed in the model and data at 7 kHz (at $-70°$) and at higher frequencies. For an array of omnidirectional sources, the grating lobe and main lobe peaks have identical levels. When the individual elements are not omnidirectional, their beampattern affects (here reduces) the grating lobe peak. The grating lobe peak levels are reasonably well predicted by the model.

The model predicts -30 dB sidelobes near nadir, as specified by the Chebyshev weights. If the TX elements were omnidirectional, sidelobe levels would be constant across angle and frequency. However, here, sidelobe levels are further reduced by the frequency and angular dependence of the individual TX elements (see Fig. 3). At some frequencies, for example, 6–7.5 kHz, the SNR in Fig. 4 is sufficiently high that the measured sidelobes follow the model, decreasing away from nadir. This gives some independent credence to the single-element beampattern.

It can be noted that when the SNR is sufficiently high, fluctuations in the measured SL sidelobes sometimes cover roughly the same range as the peak-to-null fluctuations in the model (which have a commensurate 200 Hz averaging). This can be seen, for example, between –30° and 30° from 5–7 kHz in Fig. 4. The randomness of the measured sidelobe fluctuations is due to phase and amplitude mismatches in the transducers (e.g., as presented in [13]) as well as the fact that the angular resolution at these frequencies is not sufficient to resolve the oscillations.

Results for the other TX modes, 1TX full-aperture, and 3TX half-aperture and full aperture are similar, with generally good comparison between the model and data in the main lobe, the grating lobes, and sidelobes (see Appendix).

III. Seabed Wide-Angle Reflection Coefficient Measurements

With the TX radiation pattern measured, we now proceed to the reflection coefficient measurements. The measurement geometry is quite simple—its simplicity, indeed, is one of the attractions of this measurement method. A single element on the hull-mounted source is employed with a single off-board receiver, as shown in Fig. 5. The receiver could either be moored (as shown) or drifting. In the experiments described here, a bottom mooring was employed, with the hydrophone at a height above the seabed such that the seabed reflected path is temporally separable from the direct and sea surface paths. The data processing for this geometry is described in [14]. One of the processing parameters is integration time, which determines the maximum depth into the seabed that the reflection coefficient interrogates. This time (depth) is limited in practice by the bottom-sea surface reflected path arrival time.

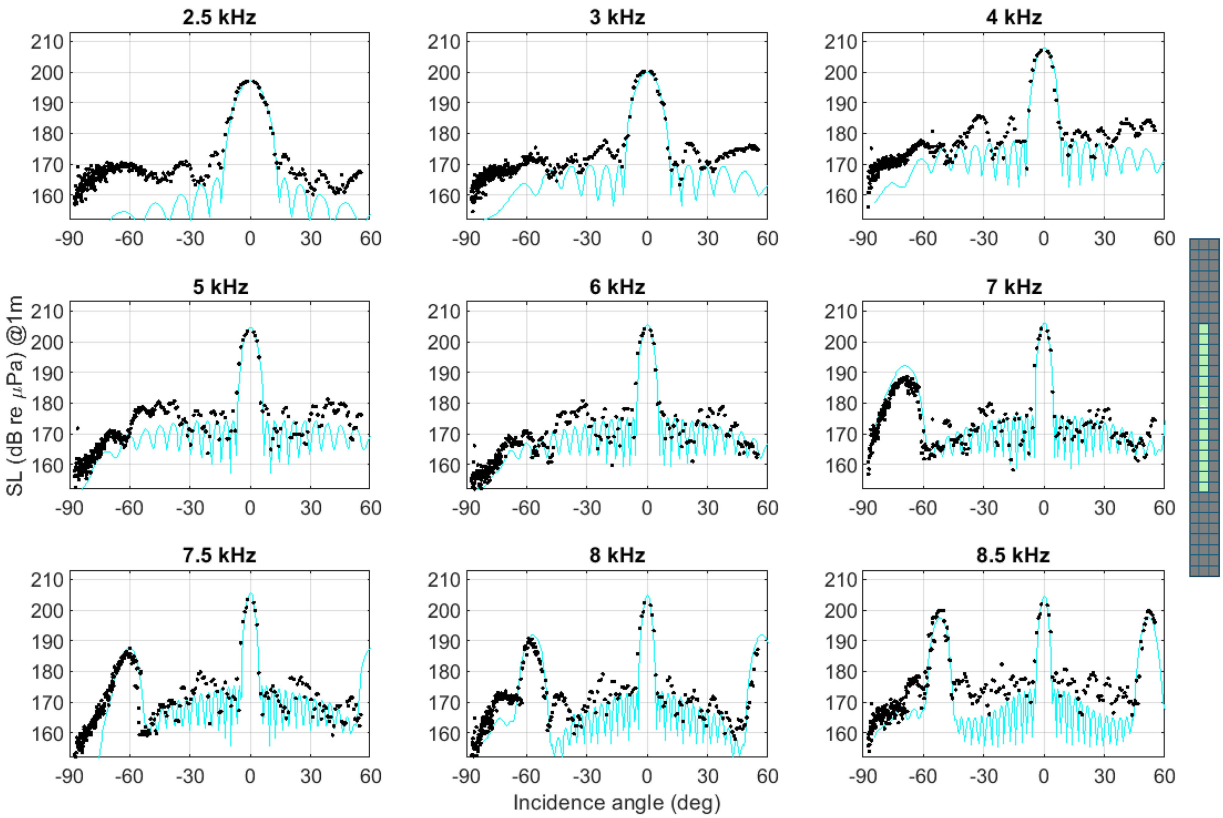

Fig. 4. Along-track source levels measured (•) at 55 V_{rms} for 1TX column at half-aperture. The model (—) is also shown. The panel to the right shows the active transmit elements of the SBP29 sonar.

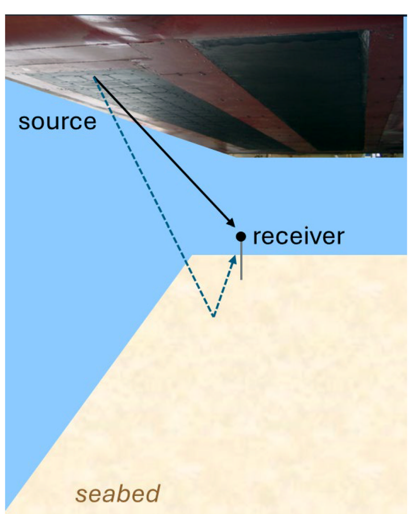

Fig. 5. Wide-angle seabed reflection coefficient at a single angle/offset. The SBP29 source is the black array on the left. Photograph courtesy of Kongsberg Discovery.

For the reflection coefficient model, the experimental geometry indicates that the observable should generally be modeled as a spherical, not a plane, wave quantity. The spherical wave reflection coefficient is obtained by scaling the Sommerfeld integral by the Green's function along the reflected path (e.g., see [15] and [16]). In its essence, the field is constructed by integration over all angles for homogeneous and inhomogeneous reflected plane waves at each source-receiver range. In some geometries, e.g., when the seabed penetration depth is small relative to the water depth, and certain other conditions are met, the plane wave approximation may be used. In the two environments shown here, the spherical-wave model was employed, but the plane-wave approximation yields similar results.

Forward modeling is invaluable for identifying the physical mechanisms that govern R(θ,f) and where in frequency and angle, various mechanisms are most prominent. Forward modeling is a precursor to geoacoustic inversion, in which a rigorous exploration of the data space is performed, but which does not provide direct indications of what regions of data space are connected to which mechanisms. In this sense, forward modeling is both a precursor to and a complement to geoacoustic inversion. Performing geoacoustic inversion on these data sets is beyond the scope of the present work.

The intent of this section is to show the first wide-angle reflection coefficient measurements made with the SBP29. Reflection measurements are shown in two distinct sedimentary environments. The first is in a highly dynamic sedimentary environment on the Eel River shelf, 97-m water depth. Scattering will be shown to be important over some of the frequency-angle space. The second is in a low-energy environment with complex layering, in the Santa Barbara Basin, 576-m water depth, where scattering plays a minimal role.

This article has been accepted for inclusion in a future issue of this journal. Content is final as presented, with the exception of pagination.

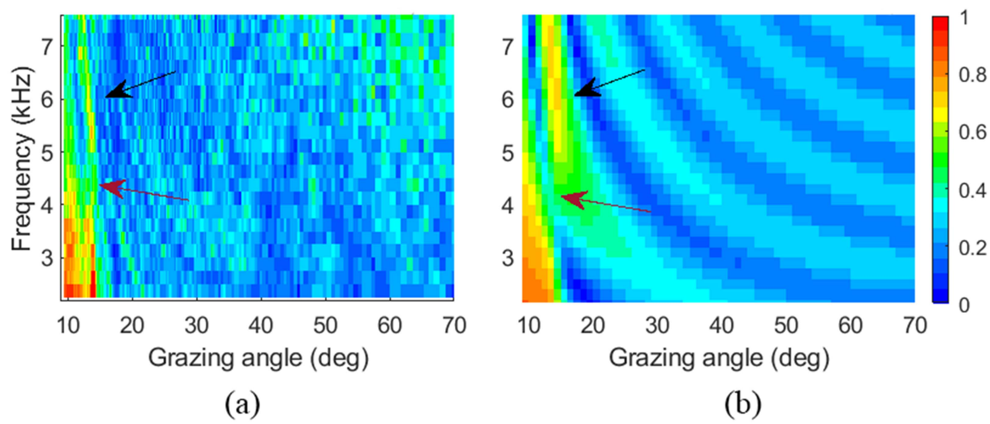

Fig. 6. Eel River shelf seabed reflection coefficient (dimensionless): (a) measured and (b) modeled. The critical angle "ridge" and "gap" discussed in the text are shown with black and red arrows, respectively.

A. *Eel River Shelf*

The Eel River Basin was extensively studied as part of the Office of Naval Research STRATAFORM (STRATA FORmation on Margins) project between 1994 and 2006 [17], [18]. STRATAFORM utilized industry multichannel seismic data and acquired geophysical data on the seafloor and shallow subsurface as well as a large number of cores [19], [20], [21], [22], [23]. Although dominated by flood-related sediment accumulation [24], the shelf also preserves the effects of storms [25] and upland land-use change [26], with an increase in fluvial sediment delivery related to natural and anthropogenic influences in the watershed [23]. In this study, we selected the outer shelf location referred to as S100 for our mooring deployment. Accumulated sediments here are characterized by a heterogeneous clayey silt (mud) characteristic of flood-produced beds. Mixing of the sediment by biological processes is also important [27], [28]. There is 10–20 m of postglacial sediment accumulation [23] with reflectors parallel to subparallel to the seafloor and evidence of gas in high-resolution seismic data [22]. It appears likely that the sediment-entrained gas is below the upper 9 m of sediment sampled by the reflection coefficient, and thus possibly does not affect the measurements. Cores in the area record 1.2–2.5 mm/yr of sediment accumulation; their age dating near the 100 m contour indicates an age of about 3000–4500 ybp (years before present) at 5 mbsf (meters below seafloor) [23]. The uppermost 50 cm in cores on the outer Eel River shelf show an increase in mud content and preserved flood-produced beds deposited after ∼1954 [23].

The reflection coefficient data, |R|, are shown in Fig. 6(a), processed at 250 Hz bandwidth with a nominal integration depth to 9 mbsf. In this section, it is convenient to use the grazing angle (instead of the incidence angle used in the SL measurements in the previous sections). One of the prominent features is the critical angle at 14° (with high |R| values), which is best observed here at low frequencies. From Snell's law and the seawater sound speed, it provides information about the basement sound speed, 1535 m/s. Another feature of interest is a "ridge" (black arrow) that starts at the critical angle just above 5 kHz and trends to ∼12° at 7.5 kHz. At slightly lower angles than the ridge, there is a "valley," a narrow, elongated feature with low amplitude, |R|∼ 0.2. At the location where that valley crosses the critical angle, 4–5 kHz, there is a "gap" (red arrow), and |R| at the critical angle drops to a low value.

TABLE I
GEOACOUSTIC PROPERTIES USED IN MODELING THE EEL RIVER REFLECTION COEFFICIENT

Thickness (m)	Sound speed (m/s)	Attenuation (dB/m/kHz)	Density (kg/m^3)
water	1487	0	1000
0.6	1495	0.1	1600
basement	1535	0.1	1800

All these features can be approximately captured with a surprisingly simple, single-layer over a halfspace geoacoustic model. The ridge and valley are interpreted to be a resonance condition (common in reflection data) due to the interference between reflected waves from the top and bottom of the layer. The ridge trajectory is where the two waves are in phase, and the valley trajectory is where the two waves are out of phase. The gap is also explained by this interference phenomenon; the basement reflected wave phase change at/near the critical angle causes the amplitude of the valley to increase, in other words, the two waves are no longer precisely out of phase.

For the ridge and valley features to be comparable to the data, the average layer sound speed appears to be between that of the water, 1487 m/s, and ∼1500 m/s. The layer thickness controls where the ridge and gap appear—a larger/smaller layer thickness moves the low-frequency end of the ridge and the low-amplitude gap lower/higher in frequency. For example, changing the layer thickness just 10 cm, from 0.6 to 0.5 m, shifts the low frequency end of the ridge from 5 kHz (consistent with the data), to nearly 6 kHz (inconsistent with the data). Thus, this layer predicts the features (ridge, gap, and valley) positions in angle and frequency reasonably well, as shown in Fig. 6(b).

What of the feature amplitudes? The amplitudes of these three features are primarily governed by the layer and basement attenuation. For example, a layer attenuation that is too low gives a ridge amplitude that is too high. A basement attenuation that is too high yields unreasonably low amplitudes below the critical

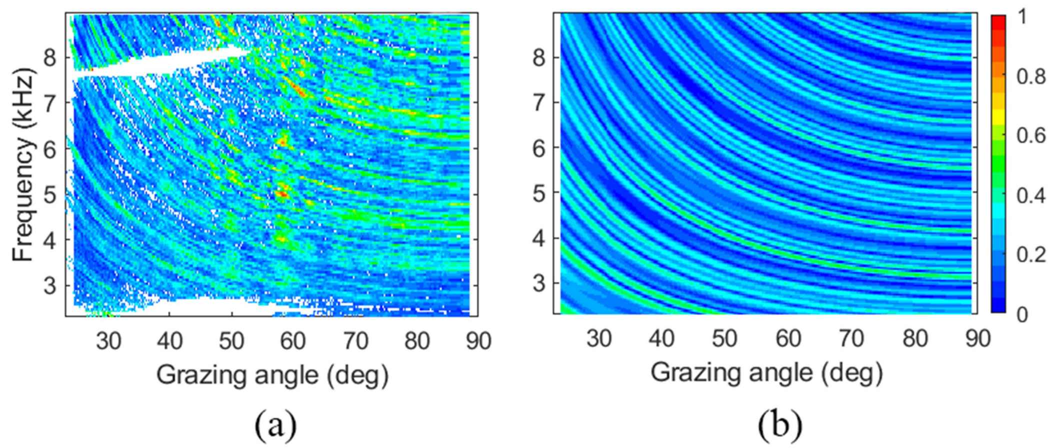

Fig. 7. Santa Barbara seabed reflection coefficient (dimensionless). (a) Measured. (b) Modeled. The regions in white have an SNR < 6 dB.

angle. These are partially correlated parameters. The density ratios (between water, layer, and basement) play a secondary role in the amplitudes. It is not the intent of the forward modeling to explore all of these, but rather to elucidate the dominant physics. Inversion methods, which are beyond the scope of this work, are well-suited to exploring the model space domain in a rigorous way. The geoacoustic model is given in Table I.

Next, grazing angles above $\sim 20°$ are explored. The model predicts an interference pattern caused by the constructive and destructive interference between waves reflected from the top and bottom of the layer. However, above $\sim 20°$, interference patterns are not readily visible in the measurements. Is this due to scattering?

The effect of scattering from interface roughness and/or sediment volume heterogeneities depends in large measure upon the size of the Fresnel zone. When the Fresnel zone is large relative to the roughness/heterogeneity scales, scattering effects on the reflected field are small. The size of the Fresnel zone depends upon both angle and frequency. The Fresnel zone is largest at low frequencies and low grazing angles. In addition, the scattering cross-section amplitude is generally smallest at low frequencies and low grazing angles. Thus, the effects of scattering on the reflection coefficient are greatest where the Fresnel zone is the smallest – at high frequencies and steep angles (the upper right corner of each plot). Thus, the forward model (which ignores scattering) captures the deterministic geoacoustic parameters only at low frequencies and low angles. At higher angles and frequencies, scattering dominates. Examples of interface scattering effects on the reflection coefficient at various roughness scales can be seen in [29] Figs. 9 and 10. Clearly, an inversion of the Eel River shelf data will require a forward model that includes both layering and roughness/volume heterogeneity, possibly including gas bubbles.

B. Santa Barbara Basin

The measurement site was near the deepest point, ~ 576 m, of the Santa Barbara Basin, southern CA, US. The basin has weak currents due to bathymetric features surrounding it that impede circulation [30]. Thus, this is a low-energy environment, where relatively flat layers would be expected. Furthermore, the restricted circulation reduces the oxygen supply to bottom waters, creating a suboxic environment [30]. This results in minimal biologic activity, which reduces or removes one process that may lead to volume heterogeneity.

TABLE II
Geoacoustic Properties Used in Modeling the Santa Barbara Basin Reflection Coefficient

Thickness (m)	Sound speed (m/s)	Attenuation (dB/m/kHz)	Density (kg/m^3)
water	*1486*	*0*	*1000*
0.9	1455	0.02	1300
2.8	1500	0.1	1700
1.5	1445	0.03	1400
0.6	1514	0.1	1900
basement	1464	0.05	1700

Annually, there are two compositionally different periods of sedimentation in the basin. During the winter, wet conditions increase terrestrial input via river discharge and sediment transport to the basin [30], [31]. During the spring/summer, strong northerly winds induce coastal upwelling, resulting in marine biogenic sediment reaching the basin [32]. Together, one terrestrial-rich and one biogenic-rich sediment lamina represent a single year [31]. In addition to the annual cycles of terrestrial and marine sediment, cores also show evidence of floods, droughts, and turbidites [30].

These processes lead to a quasi-periodic sediment structure – here expressed by a simple two-component repeating cycle of one biogenic and one terrigenous layer, with the biogenic layer having a lower sound speed, density, and attenuation. The basis of the geoacoustic model, that of a quasi-periodic sequence, was drawn from modeling sediments in abyssal plains [33]. To keep things simple and consistent with the intent of forward modeling, only two cycles (four layers) are considered (see Table II).

The measured data are shown in Fig. 7(a), processed at a 50-Hz bandwidth and with an integration depth of 45 m subbottom. Note the large number of interference fringes, indicating that many layers are contributing to the reflected field. The fringe amplitudes are largely a function of the density ratios. The arc, or trajectory across frequency and angle of a given fringe, depends on the layer sound speed. The fringe separation in frequency at a given angle is predominantly a function of the layer thickness. Note that there are various scales of interference separations, some that are close together and some that are further apart. For an example of a large-scale fringe separation, see the gap between 6 and 7 kHz at 24°.

The modeled result, Fig. 7(b), though simple, captures some basic structure of the measured data, including various scales of frequency separation in the fringes. For example, at 24°, the model shows a large gap between the fringes from 6–7 kHz, with most other fringes more closely spaced. As noted above, the measured data exhibit a gap at the same location. While this and other similarities can be noted, clearly the number of layers (fringes) in the measured data are much larger than that modeled. Nevertheless, the modeling serves to show that even a few quasi-periodic cycles can explain some trends in the data.

Several features appear in the measured data but not in the model. At 58°, high amplitude peaks, $|R|\sim0.8$ lie along some fringes. At 50°, a similar set of peaks exists at a somewhat lower amplitude. These cannot be predicted with a plane-layered model. The most likely explanation is focusing events caused by concave layers with a local radius of curvature over the Fresnel zone that matches the geometric path length at that angle. That local radius of curvature would be very large, hundreds of meters. Conversely, the low levels at 65° are probably indicative of defocusing due to a slightly convex set of layers. Since these three angles provide no additional information about the sediment properties and would increase theory error, the simplest approach for a (future) geoacoustic inversion would simply be to omit these angles. Given the wide range of angles in the data set, this would be a negligible loss of information.

C. Other Useful Quantities Requiring Radiation Patterns

In addition to the seabed reflection coefficient, other quantities of value for estimating geoacoustic information also require the absolute source level/radiation pattern. One example is frequency- and angle-dependent backscatter, from which layer roughness and volume heterogeneity information can be inferred. The full beampattern must be known from the model supported by the measurements. For example, it is known that in some instances (muddy sediments in particular) the principal scattering contribution comes from a different angle than the beam pointing angle or the nominal angle at the water-sediment interface, e.g., as presented in [34]. This occurs when the scattering mechanism is in the subbottom. Furthermore, the dominant scattering may arrive through a sidelobe and not the main lobe [34]. Thus, even knowing the main lobe beamwidth is insufficient—the full source beampattern must be modeled. Interpreting or modeling seabed bistatic scattering measurements is even more complex and also requires the full source radiation pattern in absolute levels.

The TX source level and radiation pattern model is also needed to provide quantitative insight into scattering from subbottom objects. For example, with this information, the scattering cross-section and spectral characteristics of a buried 0.22-m pipeline, as imaged by this multibeam in [5] could be examined for a deeper understanding of the physics underlying its detectability.

D. Single Element Source Modeling

The single elements were expected (modeled) to radiate as a baffled piston, which exhibits a modest variation in its beampattern. However, the single-element measured beampattern varies considerably with angle, even at the lowest frequencies. Incorporating the single-element measured beampattern into predictions of the source array largely explains the variability in the along-track grating lobe heights, as well as the frequency and angular dependence of the sidelobes, giving credence to the measurements. While the individual elements are ostensibly axisymmetric (circular), there is evidence that the beampattern is not axisymmetric, at least above ∼6 kHz.

Regarding source radiation patterns required for the reflection coefficient, the most accurate and practical approach for the foreseeable future would be measurements, not modeling. This is so because even if more element design details were known, modeling would likely not capture the significant source variability observed between two ostensibly identical elements. Furthermore, the required along-track radiation pattern measurements can be performed during the course of a reflection coefficient measurement since the experiment design ensures a temporally separable direct path.

IV. Summary and Conclusion

In the field of ocean acoustics, quantitative measurements of sediment geoacoustic properties, including sound speed, bulk density, and attenuation, are often inferred by use of calibrated, special-purpose sources. Here, the TX source level and radiation pattern of a commercial low-frequency multibeam sonar are measured, which opens the door for measuring quantities from which geoacoustic properties can be inferred. Here, the sonar is used to measure the wide-angle frequency-domain seabed reflection coefficient. Measurements were made at two locations, which have distinctly different dominant geologic, oceanographic, and biologic processes acting on the seabed.

Forward modeling reveals where high geoacoustic information exists in angle and frequency. On the Eel River shelf, the low-angle, low-frequency data provide important information about the sound speeds, attenuation, and layer thickness. At higher angles, scattering clearly dominates, with the indication that there is information about the interface roughnesses and/or volume heterogeneities. In the Santa Barbara basin, except for a few angles, the seabed can be modeled as a smooth plane-layered medium. It was shown that a simple quasi-periodic representation of the seabed captures the main features of the data. Only three cycles were required, with each cycle being defined by a low and high-speed layer (relative to the seawater sound speed).

The SBP29 source absolute levels and radiation patterns measured here are useful for wide-angle seabed reflection coefficient measurements. In addition, the modeled absolute levels are needed for calibrated seabed backscatter and bistatic seabed scatter measurements. The modeled absolute levels are also invaluable for quantitative modeling of scattering from subseabed objects, e.g., pipelines or gas plumes.

Appendix

Here, additional results related to the TX radiation patterns are provided. The survey tracks are shown in Fig. 8(a). These same tracks were executed twice, once for 1TX column and once for 3TX columns. The tracks shown are for 3TX. Fig. 8(b) shows

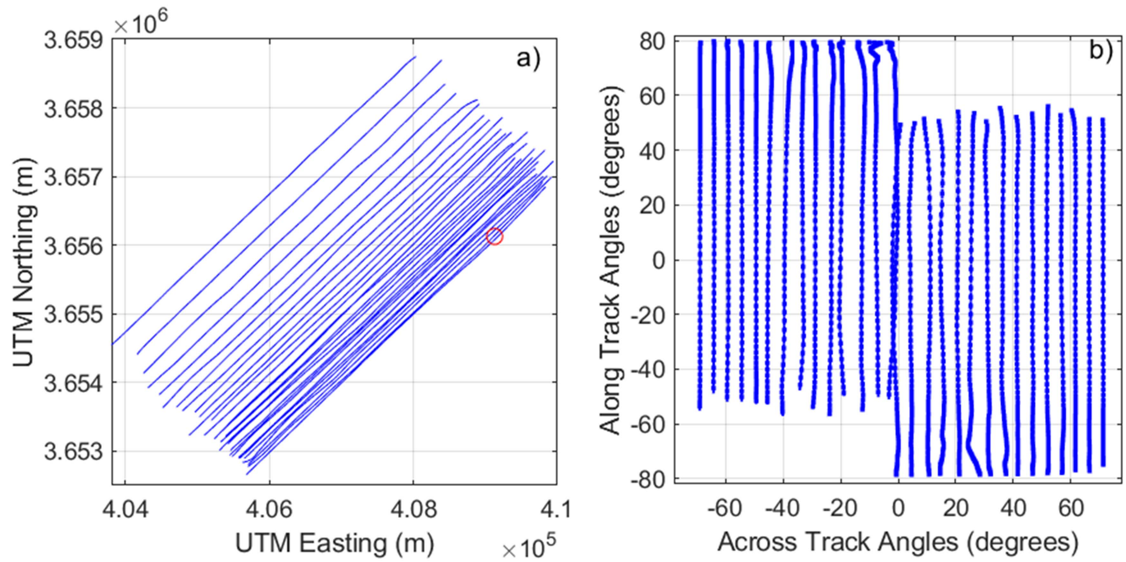

Fig. 8. Transmit calibration survey pattern. (a) Executed track lines with mooring location (°). (b) Sampled angles (•) decimated by a factor of three. The ship heading changes 180° on adjacent survey lines, which leads to sampling both port and starboard cross-track angles.

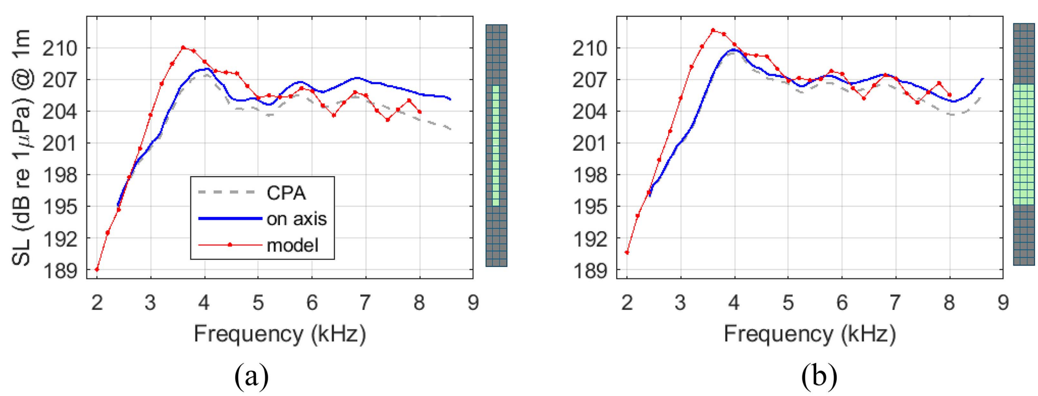

Fig. 9. On-axis source levels (SL) for half-aperture at (a) 1TX column at 55 V_{rms} and (b) 3TX columns at 27.5 V_{rms}. The panel to the right of each plot shows the active transmit elements of the SBP29 sonar.

the corresponding along- and cross-track angles. At large angles along-track, there is a higher angular resolution, simply due to geometric considerations. The higher angular resolution can be seen, for example, at angles greater than 60°.

A. On-Axis Source Level

The on-axis source levels for all array transmit modes are shown in Figs. 9 and 10 at half- and full-aperture modes, respectively. The half-aperture 1TX mode results in Fig. 9(a) are repeated from Fig. 2(b) for ease of comparison with the other three modes. The discussion, as presented in Section II-D1, pertaining to the half-aperture 1TX mode is not repeated here, but it can be seen that the model-data comparison for all four modes are broadly similar. The amplitudes between the two figures differ since the sum of the 3TX cross-track weights is $\Sigma w^{\perp} = 2.4$ and the transmit voltage for 3TX is half that of 1TX. Thus, 3TX is predicted to be $20\log10\Sigma w^{\perp})) + 20\log10(1/2)$, or 1.66 dB greater than 1TX for a given aperture. The total uncertainties of the on-axis SL include the CPA measurement uncertainties, ± 1 dB and the uncertainties of the extrapolation to on-axis. As noted in the main text, this uncertainty is a strong function of beamwidth. For the half-aperture array, the uncertainty ranges from a fraction of a dB at 2.5 kHz and increases to an estimated ± 1 dB at 8.5 kHz. For the full-aperture array, the uncertainty is considerably larger.

The full-aperture array SL was reported for the predecessor of the SBP29, the SBP120, at two frequencies, 2.5 kHz and 4 kHz [35]. Scaling those results by the difference in transmit voltage yields SL within 1 dB of the measurements in Fig. 10(b). The SL results in Fig. 10(b) above 4 kHz are considerably flatter in frequency than those reported in [36].

This article has been accepted for inclusion in a future issue of this journal. Content is final as presented, with the exception of pagination.

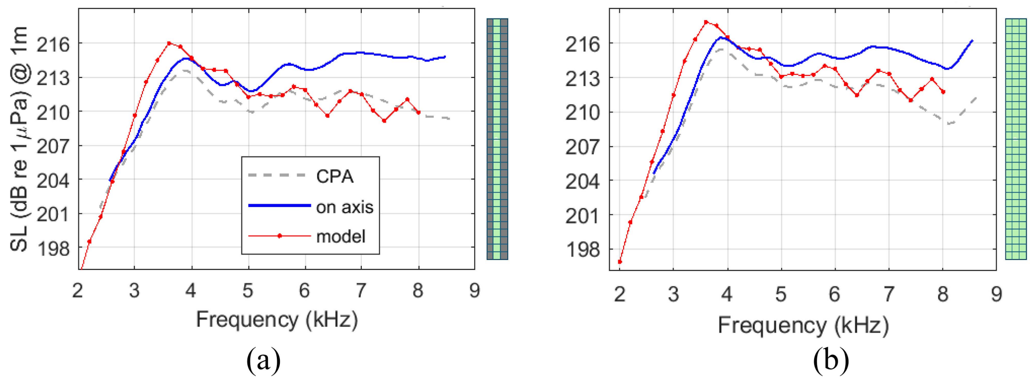

Fig. 10. On-axis source levels (SL) for full aperture at (a) 1TX column at 55 V_{rms} and (b) 3TX columns at 27.5 V_{rms}. The panel to the right of each plot shows the active transmit elements of the SBP29 sonar.

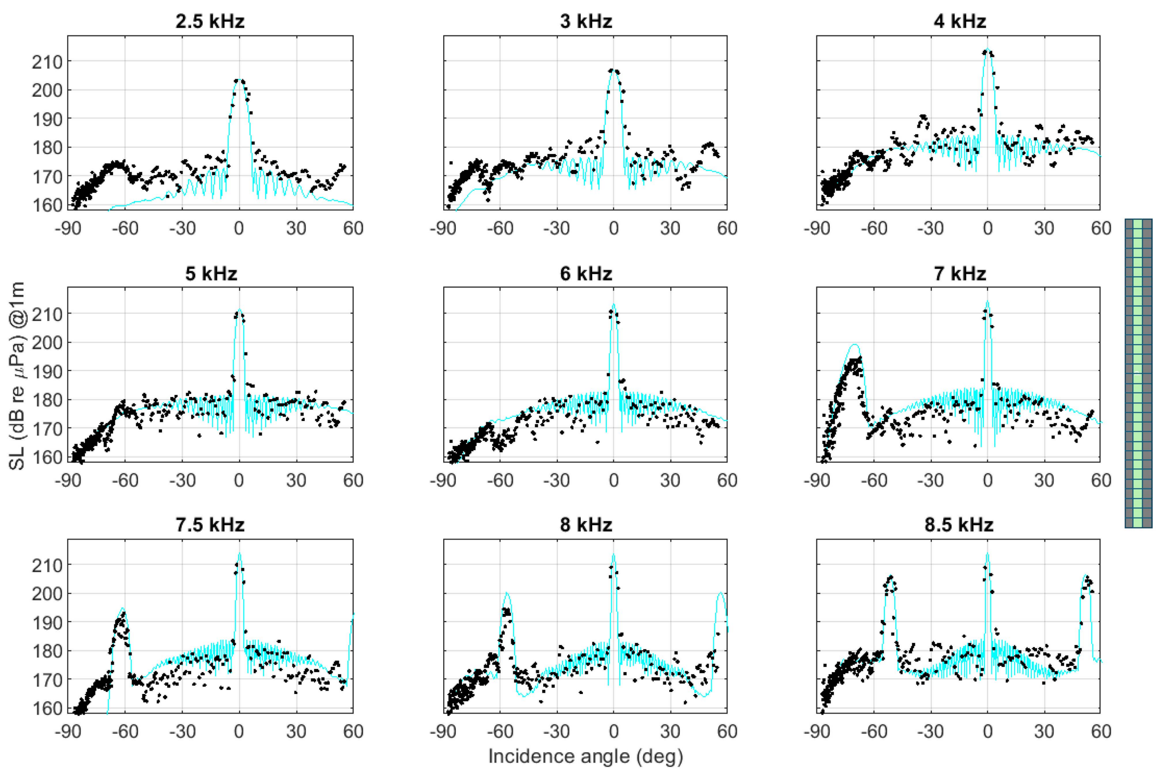

Fig. 11. Along-track measured source levels (•) at 55 V_{rms} for 1TX column at full aperture. The model (—) is also shown. The panel to the right shows the active transmit elements of the SBP29 sonar.

B. Along-track Radiation Patterns

Measured and modeled along-track SL for 1TX and 3TX are shown in Figs. 11–13. The conclusions are much the same as for the half-aperture 1TX (see Fig. 4 and discussion in the concomitant text) in that there is generally good comparison between measured and modeled data in the main lobe, the grating lobes, and the sidelobes.

C. Cross-Track Radiation Patterns

Cross-track radiation measurements were performed, consisting of 31 observations for each TX mode, that is 1 data point near CPA from each of the 31 survey lines. The cross-track data are somewhat more challenging to measure and interpret than those from along track. This is because the narrow along-track beamwidth forms a cross-track "ridge" that has to be carefully sampled. In practice, there are two issues and both lead to an underestimate of the cross-track SL: beam sampling and ship heading. Both issues primarily affect the data at high frequencies, where beamwidths are narrowest.

First, the beam sampling problem. Survey sample points generally do not fall exactly on the axis and thus under-estimate the cross-track SL. This issue was discussed in Section II-B2 for along-track data at the single CPA point. However, the

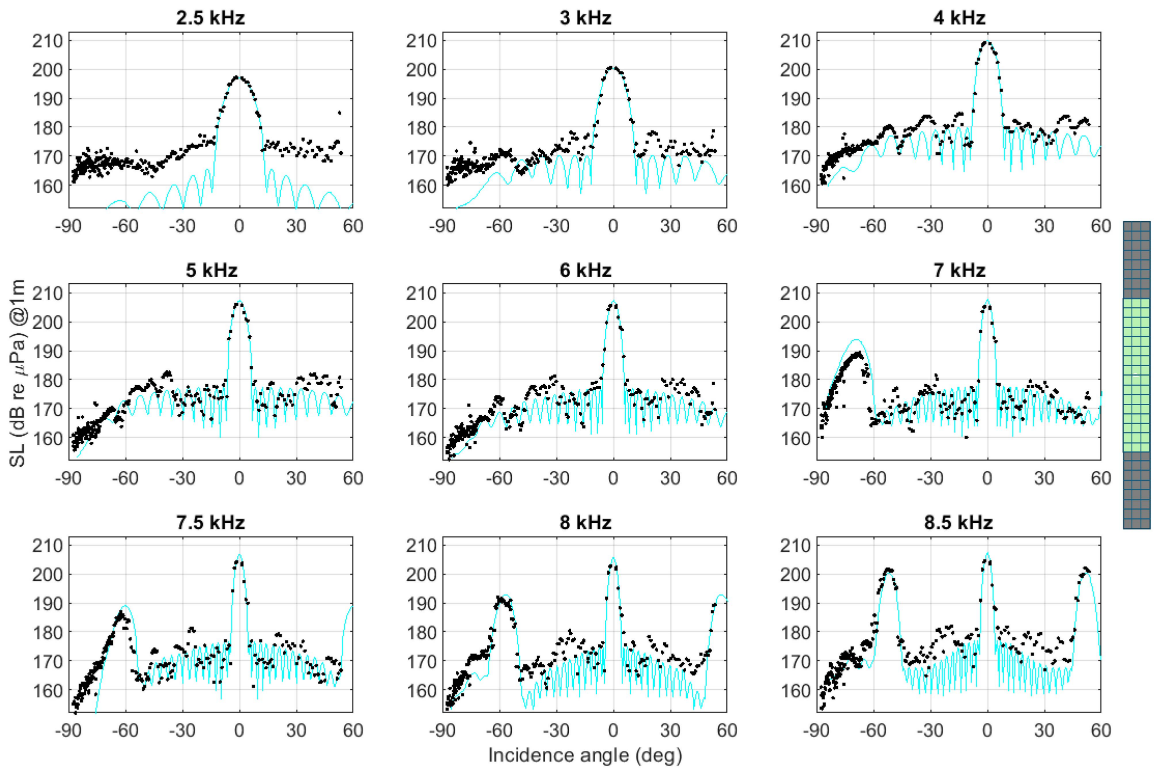

Fig. 12. Along-track measured source levels (•) at 27.5 V_{rms} for 3TX columns at half-aperture. The model (—) is also shown. The panel to the right shows the active transmit elements of the SBP29 sonar.

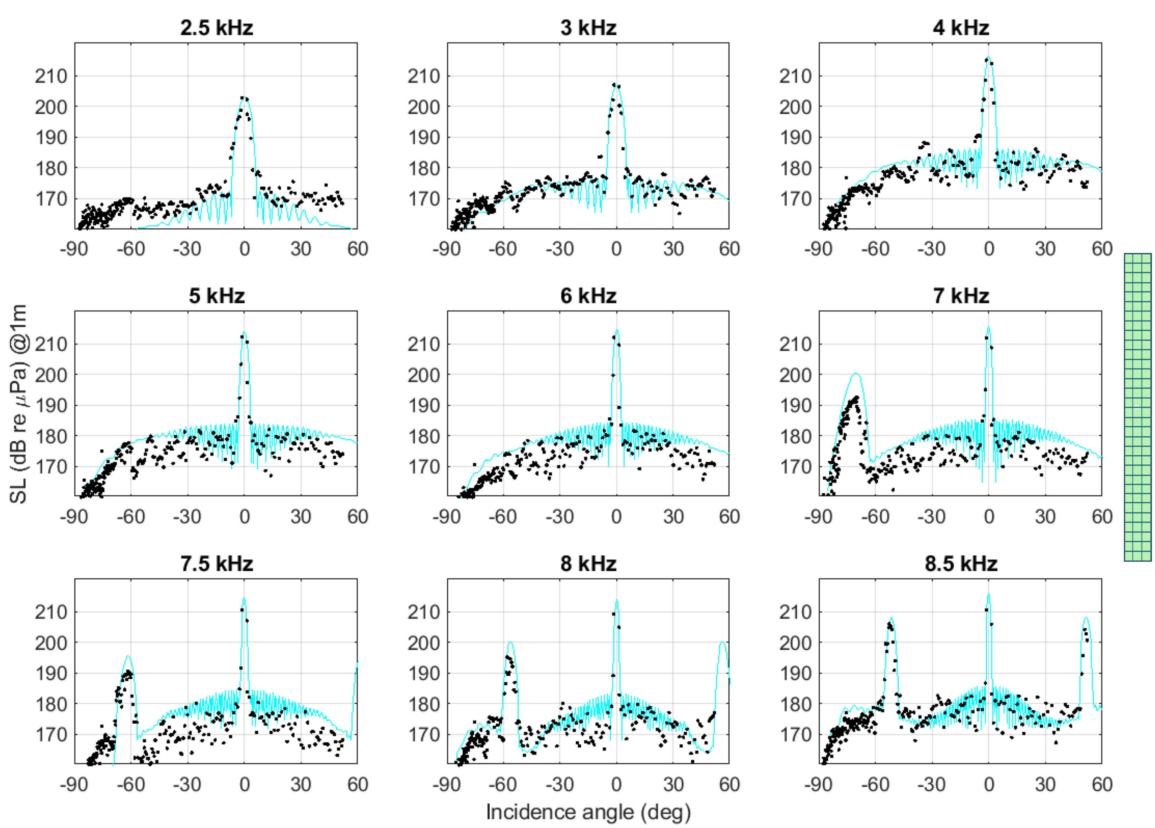

Fig. 13. Along-track measured source levels (•) at 27.5 V_{rms} for 3TX columns at full aperture. The model (—) is also shown. The panel to the right shows the active transmit elements of the SBP29 sonar.

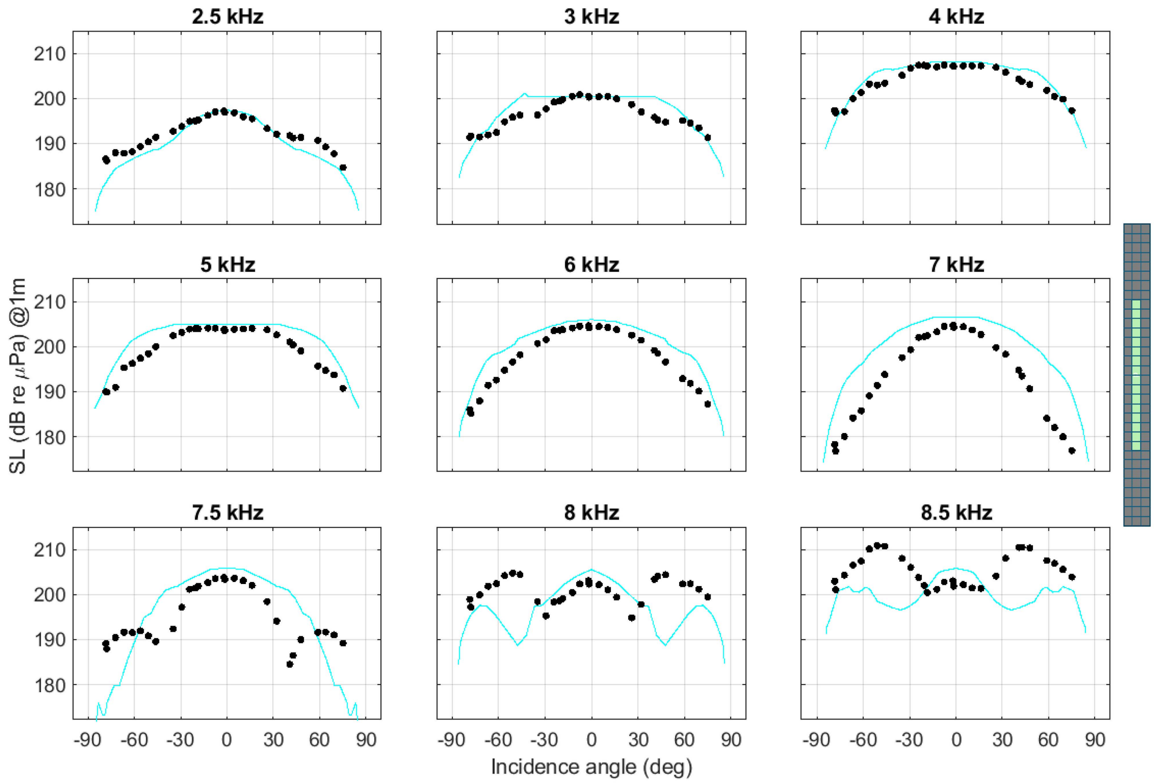

Fig. 14. Cross-track measured source levels (•) at 55 V_{rms} for 1TX column at half-aperture. The model (—) is also shown. The panel to the right shows the active transmit elements of the SBP29 sonar.

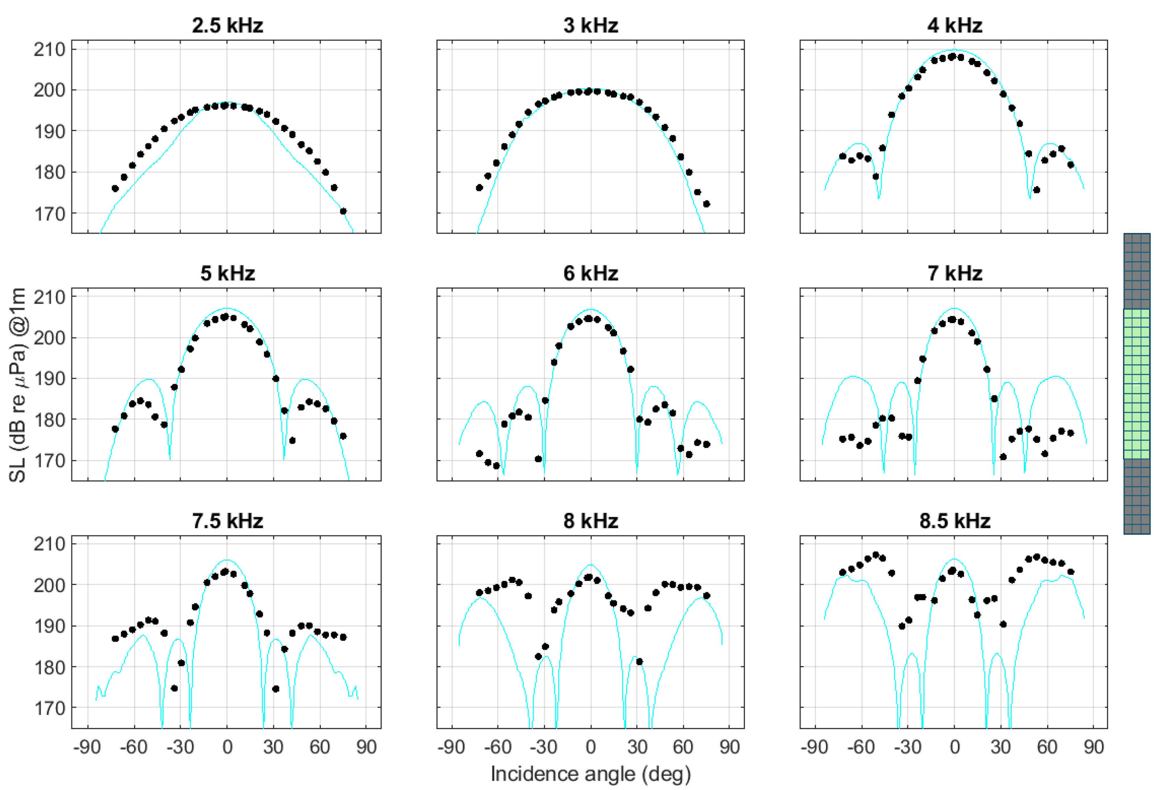

Fig. 15. Cross-track measured source levels (•) at 27.5 V_{rms} for 3 TX columns at half-aperture. The model (—) is also shown. The panel to the right shows the active transmit elements of the SBP29 sonar.

cross-track data are essentially entirely CPA points. Thus, every data point is affected by this sampling problem. As noted before, at low frequencies, the CPA and on-axis SL are virtually identical. Nevertheless, at high frequencies (narrow beamwidths) this is not the case. For example, at 8.5 kHz half-aperture, the along-track 3-dB beamwidth is 3°, and only 2–3 data points sample the 3-dB beamwidth for survey lines in the neighborhood of the receiver. At farther ranges, e.g., at 60°, the sampling improves somewhat with 5–6 data points within the 3-dB beamwidth (due to the larger beam intersection with the survey line at longer ranges). For the full array, at 8.5 kHz, where the along-track beamwidth is only 1.5°, the sampling issue is worsened.

The second and possibly more important problem is the ship heading. Due to wind, waves, and currents, the heading is typically not along the course-over-ground. This moves the on-axis position away from CPA. This is not in itself a problem. The problem is in the heading fluctuations, which shift the beam direction from ping to ping. Typically, the heading varies by 2–3° near CPA, which has little impact for a broad beam, but a large impact for a narrow beam. For example, even a small heading disparity of 1.5° from on-axis, would result in a 3 dB decrease in SL relative to on-axis at 8.5 kHz. To help mitigate heading fluctuations, the maximum SL value within ±150 m of CPA was taken. As expected, this approach yielded a more stable SL estimate than at CPA, though it does not resolve the beam sampling problem.

The radiation pattern model is based on the single element, #50, radiation pattern (see Fig. 3) scaled by the on-axis response [see Fig. 2(a)]. In other words, the single-element radiation pattern completely controls the modeled angular dependence for cross-track 1TX. This implicitly assumes that element #50 is representative of all the elements in the aperture, though it is known that on-axis differences exist and are as high as 7 dB [see Fig. 2(a)]. Differences among all transducer pairs may be even higher; however, the array response from half-aperture or full aperture would be less, due to inherent summing (averaging) across elements. The model also assumes that the beampattern, which was measured in the along-track direction, is axisymmetric.

To summarize, it is expected that the measured data should be accurate at low frequencies. But at higher frequencies, the (CPA) data will underestimate the on-axis SL, due to undersampling and fluctuating headings. The under-estimate will increase with increasing frequency and decrease somewhat with increasing angle. Two additional factors, unknown element-to-element variability (with respect to element #50) and single-element radiation pattern asymmetry, can also lead to model-data differences.

The cross-track measured and modeled data for 1TX half-aperture are presented in Fig. 14. The general trends in the model show reasonable agreement with the measured data up to 6 kHz. The model-data differences are probably related to differences in the individual TX elements, with single-element beampattern asymmetries possible.

Above 6 kHz, the model-data differences exceed 10 dB, and above 7 kHz, the overall shape of the modeled beampattern differs markedly from the measured data, most notably at 7.5 kHz, where sidelobes present in the measurements are absent in the model. This cannot be explained by individual element differences but rather suggests strong asymmetry in single-element radiation patterns between along-track and cross-track directions above 7 kHz. At and near nadir, the model-data difference above ∼6 kHz is simply because the measurement at CPA is near but not on axis and thus underestimates the SL, see discussion in Section II-B.2. This can be easily seen at nadir in the along-track data in Fig. 4 above ∼6 kHz. In other words, the measured data likely best capture the cross-track beampattern, except near nadir above ∼6 kHz, where the model is likely more accurate.

For cross-track SL with 3TX, the radiation pattern depends upon both the single-element response and the 3TX beampattern. Results are shown in Fig. 15. Note that the main lobe is much narrower than for 1TX (as expected) due to the 3TX beampattern. Another way to say this is that the single-element beampattern effects are largely masked by the narrower 3TX beampattern. Here, the main lobe is better predicted at all frequencies than for 1TX. Possible signs of single-element asymmetry are seen in frequencies higher than 7.5 kHz. These indications were also observed in the 1TX cross-track data.

Theoretically, the cross-track beampattern does not depend on the aperture size. That is, it should be the same whether for half-aperture or full aperture. Nevertheless, in practice, measuring the cross-track on-axis response becomes increasingly biased with increasing aperture (decreased beamwidth). Thus, due to beam sampling and heading fluctuations, results from the full aperture (not shown)—with on-axis beamwidths half the size of these data—show lower and more erratic cross-track source levels.

Acknowledgment

The authors gratefully acknowledge the support of the Office of Naval Research, Littoral Geosciences and Optics with Dr. Reginald Beach as a program manager. The authors would like to thank the captain, mates, and crew of the *R/V SALLY RIDE* for mooring operations and capable vessel handling as well as Mike Smith who designed the 2021 deep-water survey, Yong-Min Jiang, Laura Brownstead, and Drew Wendeborn for assistance in the reflection measurements, Stan Dosso for helpful comments on the manuscript, and Clay Whittaker for use of his SBP29 transmitter drawing.

References

[1] Y. M. Jiang, C. W. Holland, S. E. Dosso, and J. Dettmer, "Depth and frequency dependence of geoacoustic properties on the new England mud patch from reflection coefficient inversion," *J. Acoust. Soc. Amer.*, vol. 154, pp. 2383–2397, 2023.

[2] "Massa TR-1075 sub-bottom profiling transducers," MASSA Products Corporation, Hingham, MA, USA, 2012. [Online]. Available: https://www.massa.com/wp-content/uploads/2017/08/TR-1075-Datasheet-160106.pdf

[3] R. J. Stegen, "Excitation coefficients and beamwidths of Tschebyscheff arrays," *Proc. IRE*, vol. 41, no. 11, pp. 1671–1674, Nov. 1953.
[4] C. W. Holland and S. Pinson, "Sediment interval velocities from a monostatic multibeam sonar," *J. Acoust. Soc. Amer.*, vol. 147, pp. EL13–EL18, 2020.
[5] C. W. Holland, S. Pinson, D. L. Orange, and C. R. Henderson, "Cross-track seabed imaging and buried object detection with a multibeam sonar," *IEEE J. Ocean. Eng.*, vol. 50, no. 1, pp. 394–402, Jan. 2025.
[6] R. E. Francois and G. R. Garrison, "Sound absorption based on ocean measurements. Part II: Boric acid contribution and equation for total absorption," *J. Acoust. Soc. Amer.*, vol. 72, pp. 1879–1890, 1982.
[7] The MathWorks Inc., MatLab version: 9.9 (R2020b), The MathWorks Inc., Natick, MA, USA, 2020. [Online]. Available: https://www.mathworks.com
[8] M. B. Porter and H. P. Bucker, "Gaussian beam tracing for computing ocean acoustic fields," *J. Acoust. Soc. Amer.*, vol. 82, pp. 1349–1359, 1987.
[9] M. B. Porter, Ocean Acoustics Library, BELLHOP. 2025. [Online]. Available: http://oalib.hlsresearch.com/AcousticsToolbox/
[10] G. Theuillon, Y. Stéphan, and A. Pacault, "High-resolution geoacoustic characterization of the seafloor using a subbottom profiler in the Gulf of Lion," *IEEE J. Ocean. Eng.*, vol. 33, no. 3, pp. 240–254, Jul. 2008.
[11] S. E. Crocker, F. D. Fratantonio, P. E. Hart, D. S. Foster, T. F. O'Brien, and S. Labak, "Measurement of sounds emitted by certain high-resolution geophysical survey systems," *IEEE J. Ocean. Eng.*, vol. 44, no. 3, pp. 796–813, Jul. 2019.
[12] L. E. Kinsler, A. R. Frey, A. B. Coppens, and J. V. Sanders, *Fundamentals Acoust.*, 3rd ed., Hoboken, NJ, USA: Wiley, 1982, pp. 176–177.
[13] X. Lurton, "Modelling of the sound field radiated by multibeam echosounders for acoustical impact assessment," *Appl. Acoust.*, vol. 101, pp. 201–221, 2016.
[14] C. W. Holland, "Seabed reflection measurement uncertainty," *J. Acoust. Soc. Amer.*, vol. 114, pp. 1861–1873, 2003.
[15] C. W. Holland, P. L. Nielsen, J. Dettmer, and S. E. Dosso, "Resolving meso-scale seabed variability using reflection measurements from an autonomous underwater vehicle," *J. Acoust. Soc. Amer.*, vol. 131, pp. 1066–1078, 2012.
[16] L. M. Brekhovskikh and O. A. Godin, *Acoustics of Layered Media II: Point sources and Bounded Beams*. Berlin, Germany: Springer, 1999, Eq. (1.1.9).
[17] C. A. Nittrouer and J. H. Kravitz, "STRATAFORM: A program to study the creation and interpretation of sedimentary strata on continental margins," *Oceanography*, vol. 9, pp. 146–152, 1996.
[18] C. A. Nittrouer, "STRATAFORM: Overview of its design and synthesis of its results," *Mar. Geol.*, vol. 154, pp. 3–12, 1999.
[19] J. A. Goff, L. A. Mayer, J. Hughes-Clarke, and L. Pratson, "Swath mapping on the continental shelf and slope: The Eel River Basin, northern California," *Oceanography*, vol. 9, pp. 178–182, 1996.
[20] J. A. Goff, D. L. Orange, L. A. Mayer, and J. E. Hughes-Clarke, "Detailed investigation of continental shelf morphology from a high resolution swath sonar survey over the Eel River Basin, Northern California," *Mar. Geol.*, vol. 154, pp. 255–269, 1999.
[21] G. S. Mountain et al., "The long-term stratigraphic record on continental margins," in *Continental Margin Sedimentation: From Sediment Transport to Sequence Stratigraphy*. Hoboken, NJ, USA: Wiley, 2007, pp. 381–458.
[22] J. W. Yun, D. L. Orange, and M. E. Field, "Gas distribution in the Eel River Basin and its link to submarine geomorphology," *Mar. Geol.*, vol. 154, pp. 357–368, 1999.
[23] C. K. Sommerfield and R. A. Wheatcroft, "Late Holocene sediment accumulation on the Northern California shelf: Oceanic, fluvial, and anthropogenic influences," *Geol. Soc. Amer. Bull.*, vol. 119, pp. 1120–1134, 2007.
[24] R. A. Wheatcroft and J. C. Borgeld, "Oceanic flood deposits on the northern California shelf: Large-scale distribution and small-scale physical properties," *Continental Shelf Res.*, vol. 20, pp. 2163–2190, 2000.
[25] S. Fan et al., "River flooding, storm resuspension, and event stratigraphy on the Northern California shelf: Observations compared with simulations," *Mar. Geol.*, vol. 210, pp. 17–41, 2004.
[26] E. L. Leithold, D. W. Perkey, N. E. Blair, and T. N. Creamer, "Sedimentation and carbon burial on the Northern California continental shelf: The signatures of land-use change," *Continental Shelf Res.*, vol. 25, pp. 349–371, 2005.
[27] T. J. Gorgas et al., "In situ acoustic and laboratory ultrasonic sound speed and attenuation measured in heterogeneous soft seabed sediments: Eel River shelf, California," *Mar. Geol.*, vol. 182, pp. 103–119, 2002.
[28] M. D. Richardson, K. B. Briggs, S. J. Bentley, D. J. Walter, and T. H. Orsi, "The effects of biological and hydrodynamic processes on physical and acoustic properties of sediments off the Eel River, California," *Mar. Geol.*, vol. 182, pp. 121–139, 2002.
[29] C. W. Holland et al., "Seabed structure inferences from TREX13 reflection measurements," *IEEE J. Ocean. Eng.*, vol. 42, no. 2, pp. 268–288, Apr. 2017.
[30] C. T. Sarno et al., "The impacts of flood, drought, and turbidites on organic carbon burial over the past 2,000 years in the Santa Barbara Basin, California," *Paleoceanogr. Paleoclimatol.*, vol. 35, 2020, Art. no. e2020PA003849.
[31] I. L. Hendy, T. J. Napier, and A. Schimmelmann, "From extreme rainfall to drought: 250 years of annually resolved sediment deposition in Santa Barbara Basin, California," *Quaternary Int.*, vol. 387, pp. 3–12, 2015.
[32] J. A. Barron, D. Bukry, and D. Field, "Santa Barbara Basin diatom and silicoflagellate response to global climate anomalies during the past 2200 years," *Quaternary Int.*, vol. 215, pp. 34–44, 2010.
[33] C. W. Holland and G. Muncill, "Acoustic reflection from quasiperiodic sedimentary sequences," *J. Acoust. Soc. Amer.*, vol. 94, pp. 1609–1620, 1993.
[34] C. W. Holland and P. Neumann, "Sub-bottom scattering: A modeling approach," *J. Acoust. Soc. Amer.*, vol. 104, pp. 1363–1373, 1998.
[35] B. Langli and J.-C. L. Gac, "The first results with a new multibeam subbottom profiler," in *Proc. Oceans '04 MTS/IEEE Techno-Ocean '04*, 2004, vol. 2, pp. 1147–1153.
[36] A. Pacault, G. Theuillon, J.-C. L. Gac, X. Lurton, and B. Langli, "Multibeam sub-bottom profiler: Exploitation of experimental data," in *Proc. Eur. Oceans*, 2005, pp. 702–708.

Charles W. Holland received the B.S. degree in engineering from the University of Hartford, Hartford, CT, USA, in 1983, and the M.S. and Ph.D. degrees in acoustics from The Pennsylvania State University, University Park, PA, USA, in 1985 and 1991, respectively.

Between 1985 and 1996, when he was with Planning Systems Inc., he developed measurement and modeling methods for estimating seafloor properties with products for NAVOCEANO and the Fleet Air Community. From 1996 to 2001, he expanded his experimental work, developing methods for measuring shallow water wide-angle seabed reflection and scattering with the SACLANT Undersea Research Centre, La Spezia, Italy. He returned to Penn State (2001– 2020) as a Senior Scientist with the Applied Research Laboratory and a Professor of Acoustics in Penn State's Graduate Program in Acoustics with research interests in theoretical and experimental aspects of ocean acoustic propagation, reverberation, clutter, seabed reflection and scattering, and polar seismology. He is currently a Research Professor with the Department of Electrical and Computer Engineering, Portland State University, Portland, OR, USA. He authored or coauthored more than 80 peer-reviewed publications. His current research focuses on exploring new methods for inferring seabed properties using acoustic remote sensing.

Dr. Holland has been a Fellow of the Acoustical Society of America since 2006. His contributions to this work include concept generation, experiment design, data processing, theoretical analysis, manuscript preparation, and editing.

Cody R. Henderson received the B.S. degree in electrical and computer engineering and applied mathematics from Washington State University, Vancouver, WA, USA, in 2017, and the M.S. degree in signal processing and machine learning from Portland State University, Portland, OR, USA, in 2017.

He is currently an Engineer, leveraging his expertise in conducting experiments, system integration, and knowledge of underwater acoustics to develop innovative solutions for the marine industry. His current research focuses on data collection and processing.

Tim Sonnemann received the B.Sc. and M.Sc. degrees in geosciences from the University of Potsdam, Potsdam, Germany, in 2011 and 2014, respectively, and the Ph.D. degree in environmental studies from the University of Iceland, Reykjavik, Iceland, in 2019.

From 2019 to 2021, he was a Seismologist with the Icelandic Meteorological Office, Reykjavik, Iceland. After postdoctoral work from 2021 to 2022 with the University of Calgary, AB, Canada, he transferred to Portland State University, Portland, OR, USA, where he has been a Research Assistant Professor since 2024. His research interests include geophysical and geoacoustic inversion.

Dr. Sonnemann is a member of the Acoustical Society of America. His contributions include data collection.

Bjørnar Langli received the M.Sc. degree in electrical engineering and the Dr. Ing. degree in electrical engineering from the Norwegian Institute of Technology, Trondheim, Norway, in 1992 and 1997, respectively.

He is currently with Kongsberg Discovery, working with subbottom profilers. As a lead designer of the SBP-29, his contributions include implementing the single-element and single-column transmit mode and a deep understanding of the SBP29 sonar.

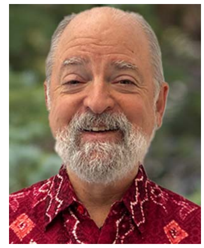

Daniel L. (DanO) Orange received the B.Sc. and M.Sc. degrees in earth and planetary sciences from Massachusetts Institute of Technology, Massachusetts, CA, USA, and the Ph.D. degree in earth sciences from the University of California, Santa Cruz, Santa Cruz, CA, USA.

After completing the Ph.D. degree in 1991, he has been entirely offshore, combining marine geology and geophysics, with a deep understanding of multibeam, to study tectonics, structural geology, geomorphology, slope failure, seepage, and process sedimentology. He has more than 28 years of industry experience in the USA and overseas, as well as academic experience primarily funded by the US Navy's Office of Naval Research. Within the industry, he has applied seafloor mapping and subbottom profiling to hydrocarbon exploration and geohazards, used process geomorphology and seismic interpretation to evaluate deepwater geohazards, and applied his knowledge of survey and navigation systems to enable the successful commercialization of controlled source electromagnetics. He is the author or coauthor of 84 peer-reviewed publications, is a coauthor of a book, and holds two patents. His contributions to this work include data collection. His research interests include subottom profiling away from nadir and comparison between the latest-generation subbottom profiling and multibeam systems with legacy hull-mounted, towed, and AUV systems.